



# High-performance light-driven heterogeneous CO<sub>2</sub> catalysis with near-unity selectivity on metal phosphides

Yang-Fan Xu<sup>1</sup>, Paul N. Duchesne<sup>1</sup>, Lu Wang<sup>1</sup>, Alexandra Tavasoli<sup>1</sup>, Feysal M. Ali<sup>1</sup>, Meikun Xia<sup>1</sup>, Jin-Feng Liao<sup>2</sup>, Dai-Bin Kuang<sup>1,2</sup>  <sup>✉</sup> & Geoffrey A. Ozin<sup>1</sup>  <sup>✉</sup>

Akin to single-site homogeneous catalysis, a long sought-after goal is to achieve reaction site precision in heterogeneous catalysis for chemical control over patterns of activity, selectivity and stability. Herein, we report on metal phosphides as a class of material capable of realizing these attributes and unlock their potential in solar-driven CO<sub>2</sub> hydrogenation. Selected as an archetype, Ni<sub>12</sub>P<sub>5</sub> affords a structure based upon highly dispersed nickel nanoclusters integrated into a phosphorus lattice that harvest light intensely across the entire solar spectral range. Motivated by its panchromatic absorption and unique linearly bonded nickel-carbonyl-dominated reaction route, Ni<sub>12</sub>P<sub>5</sub> is found to be a photothermal catalyst for the reverse water gas shift reaction, offering a CO production rate of  $960 \pm 12 \text{ mmol g}_{\text{cat}}^{-1} \text{ h}^{-1}$ , near 100% selectivity and long-term stability. Successful extension of this idea to Co<sub>2</sub>P analogs implies that metal phosphide materials are poised as a universal platform for high-rate and highly selective photothermal CO<sub>2</sub> catalysis.

<sup>1</sup> Materials Chemistry and Nanochemistry Research Group, Solar Fuels Cluster, Department of Chemistry, University of Toronto, Toronto, Ontario M5S 3H6, Canada. <sup>2</sup> MOE Key Laboratory of Bioinorganic and Synthetic Chemistry, Lehn Institute of Functional Materials, School of Chemistry, Sun Yat-sen University, 510275 Guangzhou, Guangdong, P. R. China. ✉email: [kuangdb@mail.sysu.edu.cn](mailto:kuangdb@mail.sysu.edu.cn); [g.ozin@utoronto.ca](mailto:g.ozin@utoronto.ca)

In the field of heterogeneous catalysis, gaseous or liquid reactants undergo chemical reactions on the surface of a solid material. These reactions can be enabled thermochemically, electrochemically, biochemically or photochemically<sup>1–8</sup>. The surface reactivity of catalytically active sites is typically discussed in terms of electronic, geometric and support effects<sup>9–15</sup>. Moreover, as the number of catalytically active sites scales with the surface area of the catalyst, size matters, especially at the nanoscale. Yet most heterogeneous catalysts exhibit surface structure heterogeneity that depend upon particle size and exposed facets, which influences reactivity and selectivity patterns. Furthermore, the size distribution and facet exposure can change over the course of a catalytic reaction, having a deleterious effect on selectivity patterns and long-term stability. Ideally, a heterogeneous catalyst comprised of single-size, high surface area nanoparticles, with uniform shape and facet exposure that remains stable under reaction conditions could overcome these problems; in practice however, they have rarely been achieved.

Metal phosphides form a class of solids that provide the envisioned atomic and crystalline perfection with a structure based upon highly dispersed metal nanoclusters chemically integrated in a P lattice. These materials abound with diverse stoichiometry across a wide range of metals in the periodic table offering opportunities as catalysts for electrochemical hydrogen evolution reactions, hydro-processing, and so forth<sup>16–20</sup>. However, their appealing potential for heterogeneous (photo)catalytic CO<sub>2</sub> hydrogenation remains to be unlocked.

Herein, we focus attention on an archetypal nickel phosphide, Ni<sub>12</sub>P<sub>5</sub>, with a unique surface structure based upon well-separated few-atom Ni nanoclusters. This structure allows Ni<sub>12</sub>P<sub>5</sub> to function as an exceptionally active, selective, and stable heterogeneous catalyst for the photothermal reverse water gas shift (RWGS) reaction under light stimulation. Moreover, this concept is further extended to the construction of Co<sub>2</sub>P analogs, thus revealing a bright future for the earth-abundant transition metal phosphides as a class of heterogeneous catalysts for CO<sub>2</sub> hydrogenation application. This potential is demonstrated by the high conversion rates and selectivity and long-term stability observed for these transition metal phosphides in heterogeneous CO<sub>2</sub> hydrogenation reactions driven by solar energy.

## Results

**Material synthesis and characterizations.** Nickel phosphide materials were prepared by reducing nickel phosphate oxides under H<sub>2</sub> flow. The XRD patterns, presented in Fig. 1a, showed that, in accordance with the Ni/P ratio of the chemical precursors, the as-prepared materials formed in the tetragonal Ni<sub>12</sub>P<sub>5</sub> phase. In addition, a series of SiO<sub>2</sub>-supported Ni<sub>12</sub>P<sub>5</sub> samples with different loadings (denoted by *x* wt% Ni<sub>12</sub>P<sub>5</sub>/SiO<sub>2</sub>, where the *x* is the weight percent of Ni<sub>12</sub>P<sub>5</sub> determined by ICP-OES) were prepared via wet impregnation, with XRD patterns indicating that the composition and phase remained unchanged. The as-synthesized Ni<sub>12</sub>P<sub>5</sub> exhibited a black color (Supplementary Fig. 1), and so diffuse reflectance UV-vis-NIR spectra were recorded to quantify its light absorption properties. As shown in Fig. 1b, the Ni<sub>12</sub>P<sub>5</sub> nanoparticles exhibited broadband absorption throughout UV-vis-NIR region. Loading the Ni<sub>12</sub>P<sub>5</sub> on SiO<sub>2</sub>, however, resulted in reduced optical absorption due to the dilution by the SiO<sub>2</sub> support.

The morphology and crystalline structure of the samples were subsequently characterized by transmission electron microscopy (TEM). The low-magnification TEM image (Supplementary Fig. 2b) and the corresponding particle size distribution statistics (Supplementary Fig. 3a) showed that the diameters of unsupported Ni<sub>12</sub>P<sub>5</sub> nanoparticles had a wide distribution with a mean

diameter of 86 nm. Distinctive lattice fringe spacings of 0.604 nm and 0.401 nm, with an angle of 69°, were observed in the corresponding high-resolution TEM image (Fig. 1c), which is in accordance with the (110) and (101) planes of tetragonal Ni<sub>12</sub>P<sub>5</sub>. From the TEM images of Ni<sub>12</sub>P<sub>5</sub>/SiO<sub>2</sub> samples (Supplementary Fig. 2c–e), mean particle diameters were distinctly smaller as the loading amount decreased, shrinking from about 13 nm in 10.4 wt% Ni<sub>12</sub>P<sub>5</sub>/SiO<sub>2</sub> to about 8 nm in 3.1 wt% Ni<sub>12</sub>P<sub>5</sub>/SiO<sub>2</sub> (Table 1). However, the high crystallinity was maintained, as shown by the HRTEM imaging on 10.4 wt% Ni<sub>12</sub>P<sub>5</sub>/SiO<sub>2</sub> sample (Fig. 1d), and its tetragonal phase was again confirmed by the observation of lattice spacings corresponding to the (112) and (330) planes.

X-ray photoelectron spectroscopy (XPS) was further performed to characterize the chemical states of the Ni<sub>12</sub>P<sub>5</sub> surface. As shown in Supplementary Fig. 4a, the high-resolution Ni 2p region of the pristine Ni<sub>12</sub>P<sub>5</sub> sample, before the photocatalytic reaction, consisted of two characteristic peaks located at 852.6 eV and 869.6 eV, which could be indexed to near zero-valent nickel. For the P 2p region (Supplementary Fig. 4b), two peaks were observed at 129.5 eV and 130.3 eV, and could be assigned to near zero-valent phosphorus. These values are in accordance with those reported in the literature<sup>21,22</sup>. Moreover, it is worth noting that the binding energy of Ni 2p<sub>3/2</sub> is slightly higher than that of metallic Ni, while the P 2p<sub>3/2</sub> binding energy is correspondingly lower than that of elemental P, thus indicating that Ni and P were partially positively and negatively charged, respectively, in Ni<sub>12</sub>P<sub>5</sub>.

**X-ray absorption spectroscopy measurements.** To further explore the structural features of Ni<sub>12</sub>P<sub>5</sub>, X-ray absorption spectroscopy measurements were conducted. As shown in the Ni K-edge X-ray absorption near-edge structure (XANES) spectra (Fig. 2a), the position and low intensity of the white line reveal the largely metallic character of Ni<sub>12</sub>P<sub>5</sub>, especially relative to the shifted and very intense peak observed for the strongly ionic NiO reference. These results thus provide very strong evidence supporting the low oxidation state of Ni atoms in Ni<sub>12</sub>P<sub>5</sub>. The bonding environment in Ni<sub>12</sub>P<sub>5</sub> was further investigated using extended X-ray absorption fine structure (EXAFS) analysis. As shown in Fig. 2b, two coordination shells centered at 0.163 nm and 0.264 nm were observed in the Fourier-transformed Ni K-edge EXAFS spectra of Ni<sub>12</sub>P<sub>5</sub>, which resulted from Ni–P and Ni–Ni scattering paths, respectively. The dramatically reduced Ni–Ni bond peak in Ni<sub>12</sub>P<sub>5</sub> relative to that of the Ni foil implied that the number of direct Ni–Ni bonds was reduced, due to the preferred formation of Ni–P bonds. Further curve-fitting results (Supplementary Table 1) indicated that Ni–Ni bond length was stretched from 2.480 Å in Ni foil to 2.510 Å in Ni<sub>12</sub>P<sub>5</sub>, and that the coordination number was significantly decreased from 12 in bulk Ni to 7 ± 1 in Ni<sub>12</sub>P<sub>5</sub>, which is in accordance to its theoretical crystal structure<sup>23</sup>. Thus, these EXAFS fitting results strongly support the formation of well-dispersed, low-coordinate Ni nanoclusters with slight structural distortions relative to the bulk metal.

**Photocatalytic performance.** Testing of photocatalytic CO<sub>2</sub> hydrogenation by Ni<sub>12</sub>P<sub>5</sub> catalysts was performed in a batch reactor, with samples loaded onto a borosilicate glass microfiber filter. The reaction was conducted under an initial total pressure of 18 psi (about 1.2 bar, CO<sub>2</sub>/H<sub>2</sub> = 5:1), with a light intensity of 2.3 W cm<sup>–2</sup> provided by an unfiltered Xe lamp. No external heating was adopted when using the batch reactor. Following completion of the photocatalytic reaction, products were quantified via gas chromatography. According to the GC traces (Supplementary Fig. 5), the product contained CO and a tiny

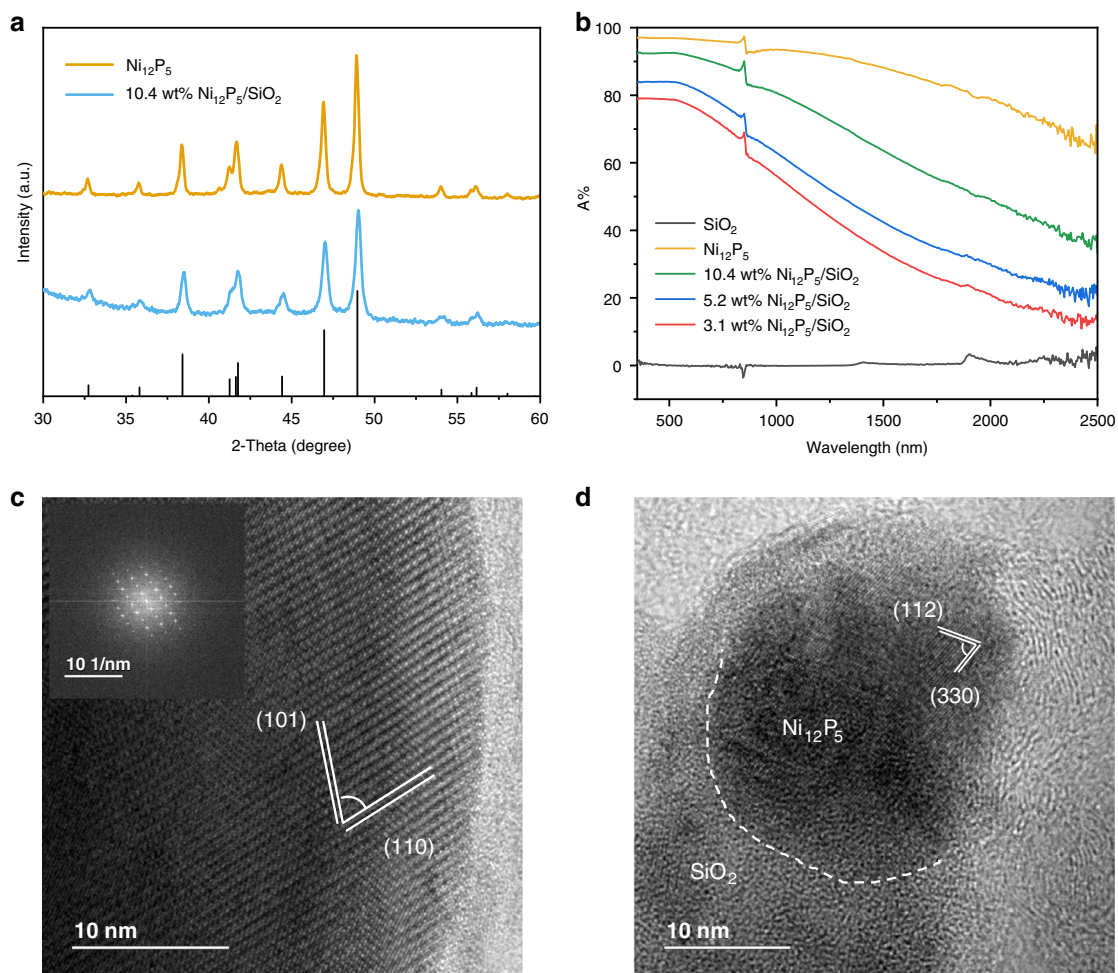


**Fig. 1** Characterization of  $\text{Ni}_{12}\text{P}_5$  nanoparticles and the 10.4 wt%  $\text{Ni}_{12}\text{P}_5/\text{SiO}_2$  nanocomposite. **a** XRD patterns, black lines indicate the standard peaks of tetragonal  $\text{Ni}_{12}\text{P}_5$  (PDF#74-1381). **b** UV-vis-NIR spectra of  $\text{Ni}_{12}\text{P}_5$ ,  $\text{SiO}_2$  and  $\text{Ni}_{12}\text{P}_5/\text{SiO}_2$  samples loaded onto a binder-free borosilicate glass microfiber filter support ( $0.5 \text{ mg cm}^{-2}$ ). **c** HRTEM image of  $\text{Ni}_{12}\text{P}_5$ , inset is the corresponding FFT electron diffraction pattern. **d** HRTEM image of 10.4 wt%  $\text{Ni}_{12}\text{P}_5/\text{SiO}_2$  composite.

**Table 1** Summary of properties and catalytic performances of representative  $\text{Ni}_{12}\text{P}_5$  samples.

Sample	$\text{Ni}_{12}\text{P}_5$ TEM mean particle size (nm)	CO rate ( $\text{mmol g}_{\text{cat}}^{-1} \text{ h}^{-1}$ )	CO selectivity (%)
$\text{Ni}_{12}\text{P}_5$	$86 \pm 30$	$156 \pm 3$	$99.5 \pm 0.1$
10.4 wt% $\text{Ni}_{12}\text{P}_5/\text{SiO}_2$	$13 \pm 7$	$960 \pm 12$	$99.7 \pm 0.1$
5.2 wt% $\text{Ni}_{12}\text{P}_5/\text{SiO}_2$	$9 \pm 3$	$678 \pm 13$	$99.7 \pm 0.1$
3.1 wt% $\text{Ni}_{12}\text{P}_5/\text{SiO}_2$	$8 \pm 4$	$334 \pm 10$	$99.7 \pm 0.1$

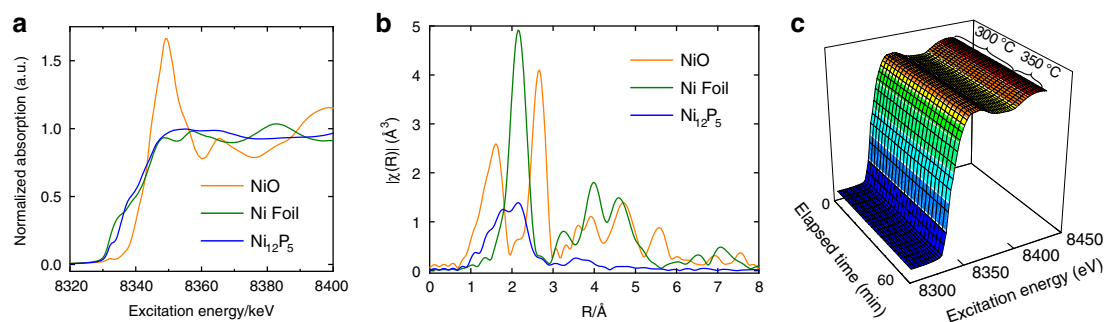


**Fig. 2** XAS measurements. **a** Ni K-edge X-ray absorption near-edge structure (XANES) spectra, with Ni Foil and NiO powder included as references. **b** R-space spectra. **c** Time-resolved in situ XANES curves plotted in the simulated reaction condition ( $\text{CO}_2:\text{H}_2 = 5:1$  gas flow, with a temperature of 300 °C or 350 °C).

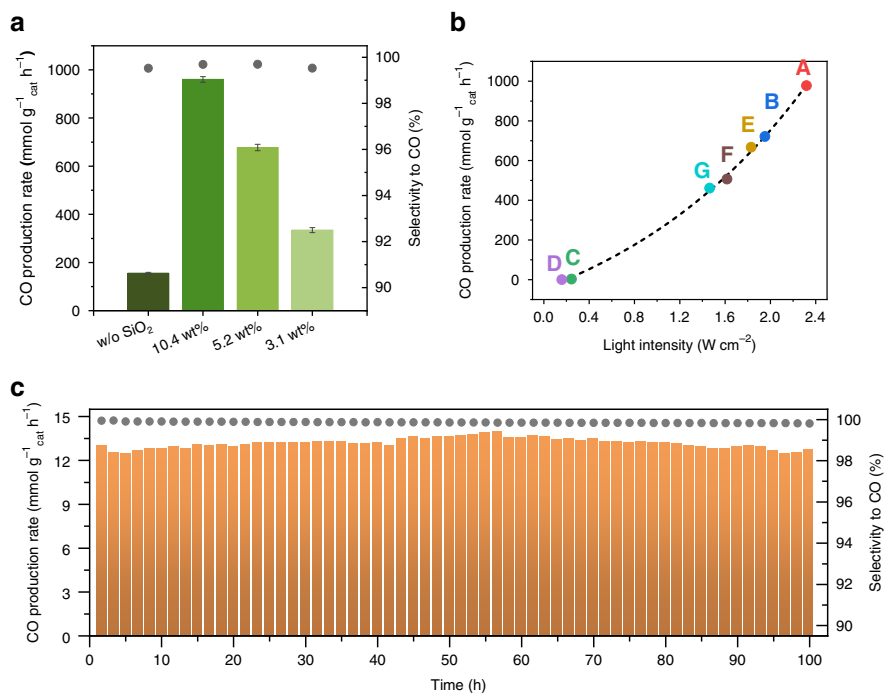


**Fig. 3** Light-driven RWGS reaction testing over Ni<sub>12</sub>P<sub>5</sub> and Ni<sub>12</sub>P<sub>5</sub>/SiO<sub>2</sub>. **a** CO production rate and selectivity as a function of catalyst loading, tested in a batch reactor under 2.3 W cm<sup>-2</sup> illumination without external heating, the initial reactant comprise 15 psi of CO<sub>2</sub> and 3 psi of H<sub>2</sub> (total pressure of 1.2 bar). Error bars are based on standard division. **b** CO production rates plotted as a function of light intensity as controlled by (A) full-spectrum light without any filter, (B) a neutral-density (ND) 0.1 filter, (C) a ND 0.3 filter, (D) a ND 0.5 filter, (E) a 420 nm cut-off filter, (F) a 495 nm cut-off filter and (G) a 590 nm cut-off filter, tested in a batch reactor. **c** Long-term stability testing over 10.4 wt% Ni<sub>12</sub>P<sub>5</sub>/SiO<sub>2</sub> in a flow reactor, under both 0.8 W cm<sup>-2</sup> light illumination and thermal activation, with 2.5 sccm of CO<sub>2</sub> and 0.5 sccm of H<sub>2</sub> gas flow.

amount of CH<sub>4</sub>, other products such as paraffin/olefin and methanol were not observed.

As summarized in Table 1 and plotted in Fig. 3a, a selectivity of 99.5% towards the RWGS route was observed, with an average CO production rate of 156 ± 3 mmol g<sub>cat</sub><sup>-1</sup> h<sup>-1</sup> being attained over unsupported Ni<sub>12</sub>P<sub>5</sub> nanoparticles. Loading the Ni<sub>12</sub>P<sub>5</sub> onto SiO<sub>2</sub> further accelerated the photocatalytic reaction rate, and a maximum rate of 960 ± 12 mmol g<sub>cat</sub><sup>-1</sup> h<sup>-1</sup> was achieved by the optimized 10.4 wt% Ni<sub>12</sub>P<sub>5</sub>/SiO<sub>2</sub> sample. This corresponds to a 5.2-fold enhancement that is quite reasonable, given that the correspondingly smaller particle size would enlarge the specific surface area and expose more accessible reaction sites per gram of catalyst, as observed from the Ni dispersion results (Supplementary Note 1). However, further lowering the loading amount results in a decrease of the CO production rate along with the turnover frequency value (for calculation details see Supplementary Note 1). One plausible explanation is the inferior light harvesting ability on lower loading samples (Fig. 1b).

As summarized in Supplementary Table 2, this rate of CO<sub>2</sub> hydrogenation to CO is a strong competitor to other reported photothermal catalysts, such as the commercial iron-chrome based catalyst, which delivered a CO production rate of 63.0 mmol g<sub>cat</sub><sup>-1</sup> h<sup>-1</sup> under the same test conditions. It should also be emphasized that selectivity toward the RWGS reaction was unchanged for the SiO<sub>2</sub>-supported Ni<sub>12</sub>P<sub>5</sub> samples, remaining at around 99.7%. Subsequent photocatalyst recyclability tests indicate that both the yield and selectivity were well retained over eight sequential runs (Supplementary Fig. 6), and XRD patterns from the spent sample confirmed that no Ni metal emerged following photocatalytic testing (Supplementary Fig. 7). XPS plots of the spent Ni<sub>12</sub>P<sub>5</sub> sample following photocatalytic testing were also recorded and showcased identical binding energies for both Ni 2p and P 2p, confirming that the oxidation

state of both Ni and P elements remained unchanged at the Ni<sub>12</sub>P<sub>5</sub> surface. To more closely monitor catalyst stability under simulated RWGS reaction conditions, time-resolved in situ XANES tests were performed under a 1:5 (v/v) flow of H<sub>2</sub>/CO<sub>2</sub> gas at 300 °C over a 40 min period. Again, no significant changes were observed in the time-resolved XANES spectra (Fig. 2c), even after further increasing the temperature to 350 °C for another 20 min, thus confirming the high stability of Ni<sub>12</sub>P<sub>5</sub> in the RWGS reaction.

Isotope tracing experiments were further conducted by replacing the normal <sup>12</sup>CO<sub>2</sub> reagent gas with isotopically labeled <sup>13</sup>CO<sub>2</sub> and using gas chromatography–mass spectrometry (GC–MS) to analyze the chemical products. As shown in Supplementary Fig. 8, the signal corresponding to <sup>13</sup>CO (*m/z* = 29) in the mass spectrum clearly confirmed that the product CO originated from the CO<sub>2</sub> feedstock rather than any carbon contaminants.

To elucidate the role of light in the catalytic performance of Ni<sub>12</sub>P<sub>5</sub>, a series of photocatalytic tests was first conducted under various light intensities by employing a set of neutral-density filters and high-pass cut-off filters. As plotted in Fig. 3b, both visible and NIR light were able to activate the Ni<sub>12</sub>P<sub>5</sub> catalyst and promote the RWGS reaction. The plot of CO production rate versus light intensity was well fitted by an exponential function, indicating a predominantly photothermal mechanism, where the catalyst absorbs and convert the incident photon flux into heat to drive the subsequent catalytic reactions<sup>24</sup>. This is distinct to the photochemical process in which the chemical reaction is driven directly by the photo-generated charge carriers, and the reaction rate would usually scale with the light intensity. Furthermore, as shown in Supplementary Note 2, the internal quantum yield (IQY) was estimated, indicating a trend that lower Ni<sub>12</sub>P<sub>5</sub> loading samples delivered inferior IQY values. As mentioned, this could

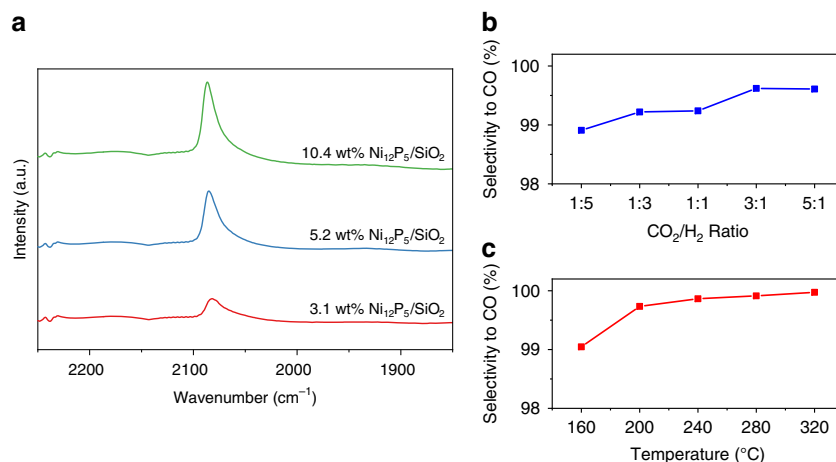


**Fig. 4** Determination of reaction pathway. **a** In situ DRIFTS spectra of Ni<sub>12</sub>P<sub>5</sub>/SiO<sub>2</sub> samples with different loading amount. **b** The selectivity to the RWGS reaction over 10.4 wt% Ni<sub>12</sub>P<sub>5</sub>/SiO<sub>2</sub> sample, plots with respect to the CO<sub>2</sub>/H<sub>2</sub> initial ratio, tested in a batch reactor under 2.3 W cm<sup>-2</sup> illumination without external heating. The initial total pressure was controlled as 18 psi (1.2 bar). **c** plots of the selectivity to the RWGS reaction over 10.4 wt% Ni<sub>12</sub>P<sub>5</sub>/SiO<sub>2</sub> sample with respect to the temperature, tested in a flow reactor under 0.8 W cm<sup>-2</sup> illumination and a gas flow of CO<sub>2</sub> (2.5 sccm) and H<sub>2</sub> (0.5 sccm).

relate to the light harvesting ability as better light absorption would contribute to a higher local temperature under light stimulation, and therefore a superior TOF value. Nevertheless, the IQYs of Ni<sub>12</sub>P<sub>5</sub> and 10.4 wt% Ni<sub>12</sub>P<sub>5</sub>/SiO<sub>2</sub> are quite close. Considering only about one tenth of the active Ni<sub>12</sub>P<sub>5</sub> has been utilized in the 10.4 wt% Ni<sub>12</sub>P<sub>5</sub>/SiO<sub>2</sub> sample when compared to pristine Ni<sub>12</sub>P<sub>5</sub>, it is conceivable that the former would be more competitive overall, especially if the system was to be scaled-up. The photothermal effect on 10.4 wt% Ni<sub>12</sub>P<sub>5</sub>/SiO<sub>2</sub> sample was further quantified by using ASPEN Plus software to estimate the local temperature of the catalyst surface based on the experimentally measured CO<sub>2</sub> conversion at reaction equilibrium<sup>4</sup>. Under 2.3 W cm<sup>-2</sup> irradiation and using a 5:1 ratio of CO<sub>2</sub>/H<sub>2</sub>, the photocatalytic reaction finally achieved 7.48% CO<sub>2</sub> conversion in the batch reactor after 11.5-h test (Supplementary Fig. 9). The corresponding predicted local temperature approached 401 °C on a wet basis and 381 °C on dry basis (Supplementary Table 3), thereby demonstrating the exceptional photothermal capabilities of Ni<sub>12</sub>P<sub>5</sub>.

**Long-term stability evaluations.** To highlight the excellent stability of Ni<sub>12</sub>P<sub>5</sub>, a 100-h long-term test was conducted in a flow reactor system in which the H<sub>2</sub> and CO<sub>2</sub> gases were continuously flowed through the catalyst and an external heat input was adopted. As shown in Fig. 3c, under a light irradiation with intensity of 0.8 W cm<sup>-2</sup> and a controlled apparent temperature of 290 °C, the 10.4 wt% Ni<sub>12</sub>P<sub>5</sub>/SiO<sub>2</sub> sample afforded an initial CO production rate and selectivity of 13.5 mmol g<sub>cat</sub><sup>-1</sup> h<sup>-1</sup> and 99.9% during the first 10 h, respectively. respectively, and only a very small decrease to 13.3 mmol g<sub>cat</sub><sup>-1</sup> h<sup>-1</sup> and 99.8% was observed after 100-h of continuous testing, thereby demonstrating its excellent long-term stability. In comparison, a control Ni/SiO<sub>2</sub> sample lost 76% of its initial CO production rate after 100 h under similar conditions and declined to a final CO selectivity of about 85% (Supplementary Fig. 10).

In addition, in the same flow reactor tests were also performed at different temperatures with and without light illumination. As shown in Supplementary Fig. 11, under thermal activation (dark conditions), the 10.4 wt% Ni<sub>12</sub>P<sub>5</sub>/SiO<sub>2</sub> sample can afford a CO production rate of 8.03 mmol g<sub>cat</sub><sup>-1</sup> h<sup>-1</sup> at 320 °C. Furthermore, the CO production rate under light conditions (i.e., both thermal and photo activation) at the same apparent temperature was 25.6 mmol g<sub>cat</sub><sup>-1</sup> h<sup>-1</sup>, corresponding to a 2.2-fold enhancement. This

enhancement was more significant at lower apparent temperature, which again indicated a solar advantage of the photothermal effect of the Ni<sub>12</sub>P<sub>5</sub> catalyst.

The TEM images of the spent photocatalysts offered further evidence of the excellent anti-sintering ability of Ni<sub>12</sub>P<sub>5</sub>/SiO<sub>2</sub>, which was conducive to its remarkable stability. As shown in Supplementary Fig. 12, the low-magnification image and particle size distribution of the Ni<sub>12</sub>P<sub>5</sub>/SiO<sub>2</sub> photocatalyst indicated that the overall mean particle size increased only slightly from about 13 nm to about 14 nm after 100 h of photocatalytic reaction. According to the corresponding HRTEM image, a high degree of crystallinity was well retained, implying the robust stability of the Ni<sub>12</sub>P<sub>5</sub> catalyst, as well as its RWGS activity. In comparison, highly dispersed Ni metal nanoparticles of about 3.3 nm in diameter were found to have strikingly grown during long-term testing, which likely accounts for its considerable performance decay (Supplementary Fig. 13). The serious sintering of metallic Ni catalysts may be related to Mond process chemistry<sup>25</sup>, in which the Ni first reacted with the product CO to form the Ni(CO)<sub>4</sub>, and at higher temperature the Ni(CO)<sub>4</sub> decomposes back to larger Ni particles. The formation of Ni(CO)<sub>4</sub> was notably significantly suppressed on nickel phosphide<sup>26,27</sup>, thus reducing the possibility of Mond process and consequent sintering.

**In situ DRIFTS studies.** In situ diffuse reflectance infrared Fourier transform spectroscopy (DRIFTS) measurements were conducted to investigate the reaction mechanism occurring at the Ni<sub>12</sub>P<sub>5</sub> surface. DRIFTS spectra were acquired at 300 °C for 1 h in CO<sub>2</sub>/H<sub>2</sub> flow after equilibrium, as presented in Fig. 4a. All DRIFT plots exhibited a pronounced peak centered at 2082 cm<sup>-1</sup> and a weak, broad peak centered at 1920 cm<sup>-1</sup>, which could be assigned to linearly bonded Ni<sup>0</sup>-CO and bridge-bonded Ni<sup>0</sup>-CO, respectively<sup>28,29</sup>. The positions of the aforementioned two peaks are the same, regardless of the loading and size of the Ni<sub>12</sub>P<sub>5</sub> particles, however, with a noticeable broadening and pronounced asymmetry of FTIR peak as the loading amount decreased, based on the FWHM analysis (Supplementary Table 4). This indicates that there is a range of surface sites for linearly bonded carbonyl species on the Ni<sub>12</sub>P<sub>5</sub> particles, likely caused by the two distinct types of Ni site in Ni<sub>12</sub>P<sub>5</sub> and their arrangements in different exposed facet<sup>30,31</sup>. Nevertheless, the intensity of the former peak overwhelms that of the latter, indicating that most carbonyl molecules preferred bonding individually to separated Ni atoms

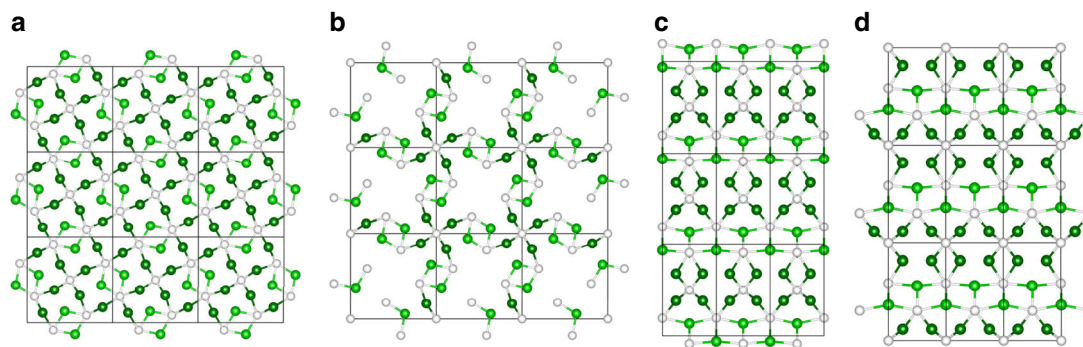


**Fig. 5** Surface crystal structure perspective of  $\text{Ni}_{12}\text{P}_5$ . **a, b** In the (001) orientation, **c, d** in (010) orientation. Note the white spheres represent the P atoms, and Ni atom with two different coordination environments are depicted as dark green and light green spheres, respectively.

over engaging in multi-coordinate bonding. Regarding the metallic Ni on which the carbonyl molecule would be bonded in both linearly and bridging modes, observations based on the DRIFTS spectra of  $\text{Ni}_{12}\text{P}_5$  implied the occurrence of unique, linearly bonded nickel-carbonyl-dominated reaction pathway. This can be explained by the ensemble effect<sup>32–34</sup>, as in this case the P atoms in  $\text{Ni}_{12}\text{P}_5$  effectively separate Ni atoms into highly dispersed nanoclusters (as depicted in the crystal structure of the  $\text{Ni}_{12}\text{P}_5$  in Fig. 5). As aforementioned, EXAFS results concluded that bonding between Ni and P resulted in an increased Ni–Ni bond length, which could geometrically hamper carbonyl bridge-bonding<sup>35,36</sup>. In addition, the absence of the fingerprint modes of formate species (as indicated in Supplementary Fig. 14) implied that the reverse water gas shift reaction over  $\text{Ni}_{12}\text{P}_5$  likely occurred through the direct  $\text{CO}_2$  dissociation route<sup>10</sup>, in accordance with reported DFT predictions<sup>37</sup>.

The merit of linearly bonded carbonyl on Ni sites lies in the relative weaker binding energy when compared to those of bridge bonded species, and would facilitate the desorption of produced CO. In addition, the decreased coordination number of metal sites (i.e., Ni in  $\text{Ni}_{12}\text{P}_5$ ) was deemed to interfere with the carbonyl dissociation and improved CO desorption<sup>38</sup>. Thereby, the consecutive reaction of CO with  $\text{H}_2$  for methane production would be hindered on the  $\text{Ni}_{12}\text{P}_5$  surface, leading to a significantly near 100% selectivity to the RWGS reaction.

## Discussion

By virtue of the well-isolated Ni nanoclusters, the linearly bonded nickel-carbonyl-dominated reaction pathway along with high RWGS reaction rate and selectivity over  $\text{Ni}_{12}\text{P}_5$  were well preserved when changing the reaction conditions. As shown in Fig. 4b and Fig. 4c, altering the initial  $\text{CO}_2$ : $\text{H}_2$  ratio (between 5:1 and 1:5) or reaction temperature (between 160 °C and 320 °C) had little influence on the selectivity. As a comparison, many studies have demonstrated that the reaction conditions, such as initial  $\text{CO}_2$ : $\text{H}_2$  ratio,  $\text{CO}_2$  conversion, temperature, catalyst particle size could significantly influence the  $\text{CO}_2$  hydrogenation selectivity over nickel related catalysts. For example, it has been reported that a higher proportion of  $\text{H}_2$  in the feed usually favors a high selectivity towards  $\text{CH}_4$  production<sup>37</sup>. Moreover, increasing the conversion of  $\text{CO}_2$  or raising the reaction temperature would also improve the selectivity to  $\text{CH}_4$  on a nickel catalyst<sup>39,40</sup>. The size of the nickel catalyst also play an important role in the reaction selectivity, where a smaller particle size would favor the formation of CO rather than  $\text{CH}_4$ <sup>10,40</sup>. The size effect was more pronounced in the case of a Ni single atom catalyst, on which the  $\text{CH}_4$  production was almost eliminated<sup>41</sup>.

In stark contrast, the observations on  $\text{Ni}_{12}\text{P}_5$  catalyst indicate that it can direct surface reaction pathways into the RWGS for

CO production, and the near 100% CO selectivity for the  $\text{Ni}_{12}\text{P}_5$  catalyst was virtually independent of overall particle size, gas composition and reaction temperature, which is a distinctive feature among nickel-containing catalyst. This unusual property thus enables  $\text{Ni}_{12}\text{P}_5$  to function as a distinctive class of RWGS catalyst and can be considered to extend Ni catalyst science and technology towards broader applicability, such as in tandem with other catalysts known for their capacity for CO conversion reactions<sup>42</sup>.

Besides  $\text{Ni}_{12}\text{P}_5$ , the metal phosphide design concept was also demonstrated in the case of a cobalt phosphide analog. As shown in Supplementary Fig. 15, the as-prepared material can be well indexed to orthorhombic  $\text{Co}_2\text{P}$ . Like  $\text{Ni}_{12}\text{P}_5$ , it is also able to absorb a wide range of the solar spectrum. In order to increase its specific area, the  $\text{SiO}_2$  supported  $\text{Co}_2\text{P}$  was also synthesized, successfully shrinking the particle size to around 14 nm (Supplementary Fig. 16). Photocatalytic reactions over  $\text{Co}_2\text{P}$  showcased a CO production rate of  $15.7 \text{ mmol g}_{\text{cat}}^{-1} \text{ h}^{-1}$  that was maintained for at least six usage cycles, and which could be further boosted to  $227.7 \text{ mmol g}_{\text{cat}}^{-1} \text{ h}^{-1}$  after loading onto  $\text{SiO}_2$  (Supplementary Fig. 17). It is worth noting that the selectivity of  $\text{Co}_2\text{P}$  toward CO was still quite high (over 99%), and exhibited the same independence of overall particle size and  $\text{CO}_2$ / $\text{H}_2$  reactant ratio effects. Similar to  $\text{Ni}_{12}\text{P}_5$ , the crystalline structure of  $\text{Co}_2\text{P}$  also displayed cobalt nanoclusters that were well-separated by P atoms (Supplementary Fig. 15d). Thus, the results presented herein over the  $\text{Co}_2\text{P}$  photocatalyst have served to further validate the metal phosphide design philosophy.

In summary, the photothermal catalytic capability of  $\text{Ni}_{12}\text{P}_5$  has been unlocked to drive a highly efficient reverse water gas shift reaction using simulated solar light, with a peak CO production rate of  $960 \pm 12 \text{ mmol g}_{\text{cat}}^{-1} \text{ h}^{-1}$  and selectivity consistently greater than 99.5%. The key to this performance lies in the ensemble effect of P, which results in the highly dispersed Ni nanoclusters in  $\text{Ni}_{12}\text{P}_5$ , and disfavored strong multi-coordinate bonding to CO. In addition, the excellent light-harvesting ability of  $\text{Ni}_{12}\text{P}_5$  across the entire solar spectrum also contributed to its photothermal activity, thereby enabling a considerably elevated local temperature to drive the RWGS reaction. Importantly, the advantages of high catalytic activity and light capture are not exclusive to  $\text{Ni}_{12}\text{P}_5$ , being shared by other transition metal phosphides such as  $\text{Co}_2\text{P}$ . Therefore, as a class of high-performance, stable and cost-effective materials, the transition metal phosphides offer interesting opportunities for the development of photothermal  $\text{CO}_2$  conversion technologies.

## Methods

**Synthesis of  $\text{Ni}_{12}\text{P}_5$  and  $\text{SiO}_2$ -supported  $\text{Ni}_{12}\text{P}_5$ .** A temperature programmed reduction (TPR) method was adopted to prepare the  $\text{Ni}_{12}\text{P}_5$  nanoparticles. In detail, nickel nitrate and ammonium phosphate,  $(\text{NH}_4)_2\text{HPO}_4$ , with molar ratio of

12:5 were first dissolved in DI water to form the precursor solution, and then dried at 120 °C, followed by annealing at 550 °C for 6 h to form nickel phosphate oxide. This precursor solid was then reduced under flowing 10 % H<sub>2</sub>/Ar at 600 °C for 6 h (with ramp of 10 °C min<sup>-1</sup> from 25 °C to 300 °C and then 2 °C min<sup>-1</sup> to 600 °C). The series of SiO<sub>2</sub>-supported Ni<sub>12</sub>P<sub>5</sub> with various catalyst loadings was prepared via incipient wetness impregnation method. In a typical synthesis, the SiO<sub>2</sub> was first immersed into a certain volume of the aforementioned precursor solution, and then followed by the same dry and H<sub>2</sub>-treatment process of the Ni<sub>12</sub>P<sub>5</sub> synthesis. In addition, a Ni/SiO<sub>2</sub> reference was also prepared in a similar impregnation route except the ammonium phosphate was not introduced into the precursor solution, and the H<sub>2</sub>-treatment temperature was 350 °C.

**Material characterization.** Powder X-ray diffraction patterns were recorded on a Bruker D2 Phaser X-ray diffractometer. UV-visible-NIR diffuse reflectance spectra were measured on Lambda 1050 UV/Vis/NIR spectrometer from Perkin Elmer, equipped with an integrating sphere. Low-resolution TEM images were taken on a FEI T12 G2 and high-resolution TEM images were taken on a Hitachi H-7650 HR-TEM. X-ray photoelectron spectroscopy (XPS) was performed on a Perkin Elmer Phi 5500 ESCA spectrometer in an ultra-high vacuum chamber, with all results being calibrated to the C 1s peaks at 284.5 eV. An Optima 7300DV ICP-OES apparatus (Perkin Elmer, USA) was used to measure the weight percent the Ni<sub>12</sub>P<sub>5</sub> content in Ni<sub>12</sub>P<sub>5</sub>/SiO<sub>2</sub> samples. Pulse H<sub>2</sub> chemisorption was performed on AutoChem II 2920 to detect the metal dispersion on each sample, assuming atomic hydrogen only binds to surface nickel atoms with a Ni/H = 1.

X-ray absorption spectroscopy measurements were performed at Sector 9-BM of the Advanced Photon Source at Argonne National Laboratory (Lemont, IL) using a Quick-EXAFS monochromator and gas-ionization chamber detectors. A specially designed sample holder/chamber was used to provide simultaneous control of atmospheric composition and catalyst temperature during in situ measurements<sup>43</sup>. The Ni<sub>12</sub>P<sub>5</sub> material was sealed in the sample chamber, purged with He and heated to 300 °C before flowing a 5:1 ratio of CO<sub>2</sub>/H<sub>2</sub> and acquiring EXAFS spectra at 30 s intervals. XANES data processing was performed using Athena, part of the Demeter software package<sup>44</sup>. Fitting of EXAFS spectra was performed using WinXAS software<sup>45</sup>, in conjunction with scattering paths generated using FEFF8<sup>46</sup> and based on crystal structures obtained from the Crystallographic Open Database<sup>47</sup>. The loading amount were calculated using ICP-AES data acquired on a Thermo iCAP 6300 spectrometer system.

**Photocatalytic gas-phase CO<sub>2</sub> reduction tests.** A batch reactor system was adopted to test the photocatalytic performance of the materials (detailed setup is shown in Supplementary Fig. 18). Before photocatalytic testing, 0.5 mg of the sample was well-dispersed in DI water via sonication and then drop-cast onto a binder-free borosilicate glass microfiber filter with an area of 1 cm<sup>2</sup> before being dried under vacuum at 80 °C. The filter-supported sample was then fixed into a custom-fabricated 11.8 mL stainless steel batch reactor with a fused silica window and finally sealed with a Viton O-ring. The reactor was then evacuated before being sequentially filled with H<sub>2</sub> and CO<sub>2</sub> gas. The total pressure of the reactants was 18 psi (about 1.2 bar), with P(H<sub>2</sub>) = 3 psi and P(CO<sub>2</sub>) = 15 psi, as monitored by an Omega PX309 pressure transducer. An unfiltered 300 W Xe lamp was employed as the light source, and the light intensity was calibrated to 2.3 W with a light meter and a mask with an area of 1 cm<sup>2</sup>. No external heating was adopted in batch reactor. Photocatalytic reactions were conducted with a duration of 0.5 h for each run, after which the product gases were separated on an SRI-8610 gas chromatograph equipped with 30 Mole Sieve 13a and 60 Haysep D columns, and then analyzed using a flame ionization detector (FID) and thermal conductivity detector (TCD). For recyclable tests, the reactor was evacuated and refilled with the reactant gases after each run, without any treatments or air (oxygen) exposure. For tests under different light intensity and wavelength range, a series neutral-density (ND) filters and high pass cut-off filters were adopted, respectively. The <sup>13</sup>C isotopic labeling experiments were also conducted in the same reactor, with the <sup>12</sup>CO<sub>2</sub> being replaced by <sup>13</sup>CO<sub>2</sub> and the products being measured on an Agilent 7890 A gas chromatograph/mass spectrometer equipped with a 60 m GS-CarbonPLOT column.

**Long-term photocatalytic gas-phase CO<sub>2</sub> reduction tests.** A flow reactor system was used for the long-term stability evaluation on the photocatalysts (detailed setup is shown in Supplementary Fig. 19). Firstly, the sample was packed into a tubular quartz capillary reactor with an inner diameter of 2 mm and an outer diameter of 3 mm. A gas flow of CO<sub>2</sub> (2.5 sccm) and H<sub>2</sub> (0.5 sccm) was then introduced into the reactor using Alicat Scientific digital flow controllers, and the temperature was regulated by an OMEGA CN616A temperature controller. The gas products were analyzed automatically on an SRI-8610, as described previously for photocatalytic activity measurements.

**In situ DRIFTS measurements.** In situ DRIFTS experiments were conducted on a Thermo Scientific Nicolet™ iS50 FT-IR Spectrometer with a HgCdTe detector. A Harrick Praying Mantis™ diffuse reflection accessory and a Harrick high-temperature reaction chamber (HTC) with ZnSe windows were employed, with an additional Harrick ATC-024-3 controller used to provide temperature control. The

samples were sealed into the sample cup and then heated to 350 °C under He flow (20 sccm) for 2 h. The samples were then cooled down to room temperature, during which time a series of background spectra were collected at different temperatures. Next, a mixture of CO<sub>2</sub>, H<sub>2</sub> and He gases was purged into the chamber using flow rates of 5, 1 and 14 sccm, respectively. Finally, spectra were collected by taking 128 scans at each different temperature stage with a resolution of 4 cm<sup>-1</sup>.

**Synthesis of Co<sub>2</sub>P and SiO<sub>2</sub>-supported Co<sub>2</sub>P.** The synthetic route used to produce Co<sub>2</sub>P is similar to that used for Ni<sub>12</sub>P<sub>5</sub>. Cobalt nitrate and (NH<sub>4</sub>)<sub>2</sub>HPO<sub>4</sub> were first dissolved in DI water at a molar ratio of 2:1, then dried and calcined at 120 °C and 550 °C, respectively. These precursor solids were finally reduced in 10% H<sub>2</sub>/Ar flow at 720 °C for 6 h (with a ramp rate of 2 °C min<sup>-1</sup> from 25 °C to 720 °C). Again, an incipient wetness impregnation route was adopted to load Co<sub>2</sub>P onto the SiO<sub>2</sub> support material.

## Data availability

The data that support the plots within this paper and other findings of this study are available from the corresponding author upon reasonable request.

Received: 24 February 2020; Accepted: 11 September 2020;

Published online: 13 October 2020

## References

1. Qian, C. X. et al. Catalytic CO<sub>2</sub> reduction by palladium-decorated silicon-hydride nanosheets. *Nat. Catal.* **2**, 46–54 (2019).
2. Li, Y. et al. Selective light absorber-assisted single nickel atom catalysts for ambient sunlight-driven CO<sub>2</sub> methanation. *Nat. Commun.* **10**, 2359 (2019).
3. Mao, C. et al. Beyond the thermal equilibrium limit of ammonia synthesis with dual temperature zone catalyst powered by solar light. *Chem* **5**, 1–16 (2019).
4. Wan, L. L. et al. Cu<sub>2</sub>O nanocubes with mixed oxidation-state facets for (photo) catalytic hydrogenation of carbon dioxide. *Nat. Catal.* **2**, 889–898 (2019).
5. Gao, D., Arán-Ais, R. M., Jeon, H. S. & Roldan Cuenya, B. Rational catalyst and electrolyte design for CO<sub>2</sub> electroreduction towards multicarbon products. *Nat. Catal.* **2**, 198–210 (2019).
6. Chen, G. et al. From solar energy to fuels: recent advances in light-driven C1 chemistry. *Angew. Chem. Int. Ed.* **58**, 17528–17551 (2019).
7. Wang, L. et al. Black indium oxide a photothermal CO<sub>2</sub> hydrogenation catalyst. *Nat. Commun.* **11**, 2432 (2020).
8. Chen, G. et al. Alumina-supported CoFe alloy catalysts derived from layered-double-hydroxide nanosheets for efficient photothermal CO<sub>2</sub> hydrogenation to hydrocarbons. *Adv. Mater.* **30**, 1704663 (2018).
9. Liu, L. & Corma, A. Metal catalysts for heterogeneous catalysis: from single atoms to nanoclusters and nanoparticles. *Chem. Rev.* **118**, 4981–5079 (2018).
10. Vogt, C. et al. Unravelling structure sensitivity in CO<sub>2</sub> hydrogenation over nickel. *Nat. Catal.* **1**, 127–134 (2018).
11. Yan, X. et al. Nickel@Siloxene catalytic nanosheets for high-performance CO<sub>2</sub> methanation. *Nat. Commun.* **10**, 2608 (2019).
12. Yan, T. et al. Polymorph selection towards photocatalytic gaseous CO<sub>2</sub> hydrogenation. *Nat. Commun.* **10**, 2521 (2019).
13. Macino, M. et al. Tuning of catalytic sites in Pt/TiO<sub>2</sub> catalysts for the chemoselective hydrogenation of 3-nitrostyrene. *Nat. Catal.* **2**, 873–881 (2019).
14. Li, Z. et al. Well-defined materials for heterogeneous catalysis: from nanoparticles to isolated single-atom sites. *Chem. Rev.* **120**, 623–682 (2020).
15. Xia, T., Long, R., Gao, C. & Xiong, Y. Design of atomically dispersed catalytic sites for photocatalytic CO<sub>2</sub> reduction. *Nanoscale* **11**, 11064–11070 (2019).
16. Shi, Y. & Zhang, B. Recent advances in transition metal phosphide nanomaterials: synthesis and applications in hydrogen evolution reaction. *Chem. Soc. Rev.* **45**, 1529–1541 (2016).
17. Oyama, S. T., Gott, T., Zhao, H. Y. & Lee, Y. K. Transition metal phosphide hydroprocessing catalysts: a review. *Catal. Today* **143**, 94–107 (2009).
18. Careno, S., Portehault, D., Boissiere, C., Mezailles, N. & Sanchez, C. Nanoscaled metal borides and phosphides: recent developments and perspectives. *Chem. Rev.* **113**, 7981–8065 (2013).
19. Cai, J. et al. N-induced lattice contraction generally boosts the hydrogen evolution catalysis of P-rich metal phosphides. *Sci. Adv.* **6**, eaaw8113 (2020).
20. Duyar, M. S. et al. A highly active molybdenum phosphide catalyst for methanol synthesis from CO and CO<sub>2</sub>. *Angew. Chem. Int. Ed.* **57**, 15045–15050 (2018).
21. Calvino, K. U. D. et al. Selective CO<sub>2</sub> reduction to C-3 and C-4 oxyhydrocarbons on nickel phosphides at overpotentials as low as 10 mV. *Energy Environ. Sci.* **11**, 2550–2559 (2018).

22. Gao, R. et al. Ultradispersed nickel phosphide on phosphorus-doped carbon with tailored d-band center for efficient and chemoselective hydrogenation of nitroarenes. *ACS Catal.* **8**, 8420–8429 (2018).
23. Larsson, E. An X-ray investigation of the Ni-P system and the crystal structures of NiP and NiP<sub>2</sub>. *Ark. Kemi* **23**, 335–365 (1965).
24. Jia, J. et al. Visible and near-infrared photothermal catalyzed hydrogenation of gaseous CO<sub>2</sub> over nanostructured Pd@Nb<sub>2</sub>O<sub>5</sub>. *Adv. Sci.* **3**, 1600189 (2016).
25. Mond, L., Langer, C. & Quincke, F. L. Action of carbon monoxide on nickel. *J. Chem. Soc. Trans.* **57**, 749–753 (1890).
26. Sawhill, S. J. et al. Thiophene hydrodesulfurization over nickel phosphide catalysts: effect of the precursor composition and support. *J. Catal.* **231**, 300–313 (2005).
27. Layman, K. A. & Bussell, M. E. Infrared spectroscopic investigation of CO adsorption on silica-supported nickel phosphide catalysts. *J. Phys. Chem. B* **108**, 10930–10941 (2004).
28. Chen, Y. D. et al. Metal phosphides derived from hydrotalcite precursors toward the selective hydrogenation of phenylacetylene. *ACS Catal.* **5**, 5756–5765 (2015).
29. Zhu, X., Huo, P., Zhang, Y.-p., Cheng, D.-g. & Liu, C.-j. Structure and reactivity of plasma treated Ni/Al<sub>2</sub>O<sub>3</sub> catalyst for CO<sub>2</sub> reforming of methane. *Appl. Catal. B* **81**, 132–140 (2008).
30. Zhao, H., Oyama, S. T., Freund, H.-J., Włodarczyk, R. & Sierka, M. Nature of active sites in Ni<sub>2</sub>P hydrotreating catalysts as probed by iron substitution. *Appl. Catal. B* **164**, 204–216 (2015).
31. Hu, J. et al. Stable active sites on Ni<sub>12</sub>P<sub>5</sub> surfaces for the hydrogen evolution reaction. *Energy Technol.* **7**, 1900013 (2019).
32. Zhong, W., Qi, Y. & Deng, M. The ensemble effect of formic acid oxidation on platinum–gold electrode studied by first-principles calculations. *J. Power Sources* **278**, 203–212 (2015).
33. Duchesne, P. N. et al. Golden single-atomic-site platinum electrocatalysts. *Nat. Mater.* **17**, 1033–1039 (2018).
34. Liu, P. & Rodriguez, J. A. Catalysts for hydrogen evolution from the NiFe hydrogenase to the Ni<sub>2</sub>P(001) surface: the importance of ensemble effect. *J. Am. Chem. Soc.* **127**, 14871–14878 (2005).
35. Popczun, E. J. et al. Nanostructured nickel phosphide as an electrocatalyst for the hydrogen evolution reaction. *J. Am. Chem. Soc.* **135**, 9267–9270 (2013).
36. Liu, P., Rodriguez, J. A., Takahashi, Y. & Nakamura, K. Water-gas-shift reaction on a Ni<sub>2</sub>P(001) catalyst: formation of oxy-phosphides and highly active reaction sites. *J. Catal.* **262**, 294–303 (2009).
37. Guharoy, U., Reina, T. R., Olsson, E., Gu, S. & Cai, Q. Theoretical insights of Ni<sub>2</sub>P (0001) surface toward its potential applicability in CO<sub>2</sub> conversion via dry reforming of methane. *ACS Catal.* **9**, 3487–3497 (2019).
38. Chen, X. et al. Theoretical insights and the corresponding construction of supported metal catalysts for highly selective CO<sub>2</sub> to CO conversion. *ACS Catal.* **7**, 4613–4620 (2017).
39. Du, G. et al. Methanation of carbon dioxide on Ni-incorporated MCM-41 catalysts: the influence of catalyst pretreatment and study of steady-state reaction. *J. Catal.* **249**, 370–379 (2007).
40. Wu, H. C. et al. Methanation of CO<sub>2</sub> and reverse water gas shift reactions on Ni/SiO<sub>2</sub> catalysts: the influence of particle size on selectivity and reaction pathway. *Catal. Sci. Technol.* **5**, 4154–4163 (2015).
41. Millet, M. M. et al. Ni single atom catalysts for CO<sub>2</sub> activation. *J. Am. Chem. Soc.* **141**, 2451–2461 (2019).
42. Ma, Z. & Porosoff, M. D. Development of tandem catalysts for CO<sub>2</sub> hydrogenation to olefins. *ACS Catal.* **9**, 2639–2656 (2019).
43. Bolin, T. B. et al. In situ intermediate-energy X-ray catalysis research at the advanced photon source beamline 9-BM. *Catal. Today* **205**, 141–147 (2013).
44. Ravel, B. & Newville, M. ATHENA, ARTEMIS, HEPHAESTUS: data analysis for X-ray absorption spectroscopy using IFEFFIT. *J. Synchrotron Radiat.* **12**, 537–541 (2005).
45. Ressler, T. WinXAS: a program for X-ray absorption spectroscopy data analysis under MS-Windows. *J. Synchrotron Radiat.* **5**, 118–122 (1998).
46. Ankudinov, A. L., Ravel, B., Rehr, J. J. & Conradson, S. D. Real-space multiple-scattering calculation and interpretation of x-ray-absorption near-edge structure. *Phys. Rev. B* **58**, 7565–7576 (1998).
47. Gražulis, S. et al. Crystallography Open Database (COD): an open-access collection of crystal structures and platform for world-wide collaboration. *Nucleic Acids Res* **40**, D420–D427 (2012).

## Acknowledgements

G.A.O. acknowledges the financial support of the following agencies: Ontario Ministry of Research and Innovation; Ministry of Economic Development, Employment and Infrastructure; Ministry of the Environment and Climate Change; Best in Science; Ministry of Research Innovation and Science Low Carbon Innovation Fund; Ontario Centre of Excellence Solutions 2030 Challenge Fund; Alexander von Humboldt Foundation; Imperial Oil; University of Toronto Connaught Innovation Fund; Connaught Global Challenge Fund and the Natural Sciences and Engineering Research Council of Canada. D.K. acknowledges the financial support from the National Natural Science Foundation of China (21875288), the GDUPS (2016). This research used resources of the Advanced Photon Source, a U.S. Department of Energy (DOE) Office of Science User Facility operated for the DOE Office of Science by Argonne National Laboratory under Contract No. DE-AC02-06CH11357. Sector 9-BM beamline scientists Tianpin Wu and George Sterbinski of the APS Spectroscopy group are thanked for their expert assistance in beamline optimization and operation. P.N.D. acknowledges financial support from the NSERC Postdoctoral Fellowships program. A. Tountas' help on ASPEN estimation is acknowledged by all authors. This paper is dedicated to Professor Geoffrey Ozin on the occasion of his 77th birthday.

## Author contributions

Y.X. and G.A.O. conceived and designed the experiments. Y.X. prepared the materials and performed the SEM, XRD, UV-vis-NIR, in situ DRIFTS and photocatalytic characterizations. L.W. performed XPS characterizations. F.M.A. and J.L. performed the TEM characterizations. M.X. performed the ICP-OES detection. A.A.T. conducted the ASPEN simulation. P.N.D. performed and analyzed the XAS experiments. J.L. and D.K. performed the pulse H<sub>2</sub> chemisorption tests. Y.X., P.N.D. and G.A.O. co-wrote the manuscript. All authors discussed the results and commented on the manuscript.

## Competing interests

The authors declare no competing interests.

## Additional information

**Supplementary information** is available for this paper at <https://doi.org/10.1038/s41467-020-18943-2>.

**Correspondence** and requests for materials should be addressed to D.-B.K. or G.A.O.

**Peer review information** *Nature Communications* thanks Mark Bussell and other, anonymous, reviewers for their contributions to the peer review of this work. Peer review reports are available.

**Reprints and permission information** is available at <http://www.nature.com/reprints>

**Publisher's note** Springer Nature remains neutral with regard to jurisdictional claims in published maps and institutional affiliations.



**Open Access** This article is licensed under a Creative Commons Attribution 4.0 International License, which permits use, sharing, adaptation, distribution and reproduction in any medium or format, as long as you give appropriate credit to the original author(s) and the source, provide a link to the Creative Commons license, and indicate if changes were made. The images or other third party material in this article are included in the article's Creative Commons license, unless indicated otherwise in a credit line to the material. If material is not included in the article's Creative Commons license and your intended use is not permitted by statutory regulation or exceeds the permitted use, you will need to obtain permission directly from the copyright holder. To view a copy of this license, visit <http://creativecommons.org/licenses/by/4.0/>.

© The Author(s) 2020